

Anticrack inclusion model for compaction bands in sandstone

Kurt R. Sternlof

Department of Geological and Environmental Sciences, Stanford University, Stanford, California, USA

John W. Rudnicki

Department of Civil and Environmental Engineering, Northwestern University, Evanston, Illinois, USA

David D. Pollard

Department of Geological and Environmental Sciences, Stanford University, Stanford, California, USA

Received 5 April 2005; revised 5 July 2005; accepted 5 August 2005; published 5 November 2005.

[1] Detailed observations of compaction bands exposed in the Aztec Sandstone of southeastern Nevada indicate that these thin, tabular, bounded features of localized porosity loss initiated at pervasive grain-scale flaws, which collapsed in response to compressive tectonic loading. From many of these Griffith-type flaws, an apparently self-sustaining progression of collapse propagated outward to form bands of compacted grains a few centimeters thick and tens of meters in planar extent. These compaction bands can be idealized as highly eccentric ellipsoidal bodies that have accommodated uniform uniaxial plastic strain parallel to their short dimension within a surrounding elastic material. They thus can be represented mechanically as contractile Eshelby inclusions, which generate near-tip compressive stress concentrations consistent with self-sustaining, in-plane propagation. The combination of extreme aspect ratio ($\sim 10^{-4}$) and significant uniaxial plastic strain ($\sim 10\%$) also justifies an approximation of the bands as anticracks: sharp boundaries across which a continuous distribution of closing mode displacement discontinuity has been accommodated. This anticrack interpretation of compaction bands is analogous to that of pressure solution surfaces, except that porosity loss takes the place of material dissolution. We find that displacement discontinuity boundary element modeling of compaction bands as anticracks within a two-dimensional linear elastic continuum can accurately represent the perturbed external stress fields they induce.

Citation: Sternlof, K. R., J. W. Rudnicki, and D. D. Pollard (2005), Anticrack inclusion model for compaction bands in sandstone, *J. Geophys. Res.*, 110, B11403, doi:10.1029/2005JB003764.

1. Introduction

[2] Compaction bands represent one kinematic end-member of the suite of structures known collectively as deformation bands, which also includes shear and dilation bands [Antonellini *et al.*, 1994; Aydin, 1978; Du Bernard *et al.*, 2002; Mollema and Antonellini, 1996]. Because of the internal loss of porosity and permeability that they accommodate, deformation bands can significantly affect bulk sandstone permeability when present as pervasive arrays, with important implications for the management of both groundwater and hydrocarbon resources [Sternlof *et al.*, 2004].

[3] The term compaction band (CB) was coined by Mollema and Antonellini [1996, p. 209] to describe "...tabular zones of localized deformation...that accommodate pure compaction" in sandstone, and which constitute "...analogs for anticracks...such as pressure solution surfaces," following the analysis of Fletcher and Pollard [1981]. Mollema and Antonellini described two types of

compactions bands (straight, thick bands and wavy, or crooked bands) both exhibiting porosity loss in the absence of shear accommodated by granular rearrangement, grain cracking, indentation and limited comminution. They identified these structures as forming primarily within the compressional quadrants of deformation band-style faults [Aydin, 1978; Aydin and Johnson, 1978] in the Jurassic aeolian Navajo Sandstone of the Kaibab Monocline in Utah, finding them to be on the order of meters in trace length, segmented, and restricted to a limited outcrop area on the downthrown limb of the monocline in relatively coarse grained, high-porosity layers.

[4] Extensive arrays of CBs pervade the upper half of the Jurassic Aztec Sandstone exposed in and around the Valley of Fire State Park of southeastern Nevada (Figure 1) where, however, they bear no immediate genetic relationship to local faults and are tens to more than one hundred meters in trace length [Sternlof *et al.*, 2004]. The Aztec is a 1400-m-thick eolian sandstone composed of greater than 90% detrital quartz and typified by large-scale tabular and trough cross bedding, average porosity of about 20%, and a mean grain diameter of about 0.25 mm within a range of about 0.1 to 0.5 mm [Flodin *et al.*, 2005]. Throughout the

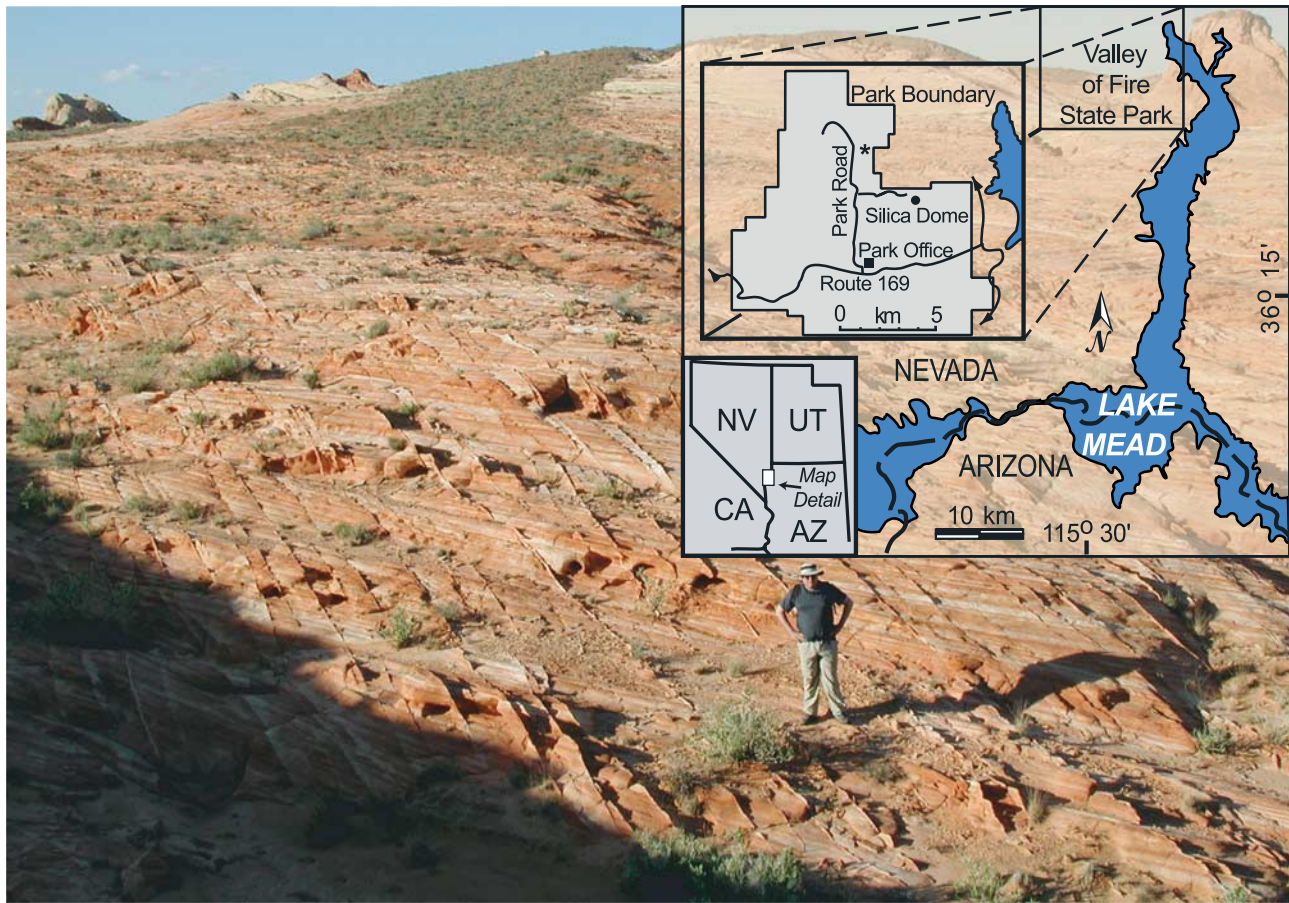


Figure 1. Location of the Valley of Fire State Park, southeastern Nevada (map inset), where more than 20 km² of the 1400-m-thick eolian Jurassic Aztec Sandstone are extensively exposed. Photo shows view northward from the location marked by asterisk on the park detail. Throughout the upper half of the Aztec, compaction bands crop out in positive relief as subparallel, centimeter-thick, north-northwest trending, steeply east dipping tabular fins spaced from centimeters to meters apart.

weakly lithified upper Aztec, two distinct phases of deformation bands are present. Steeply dipping, centimeter-thick CBs of the first phase comprise the oldest structural fabric. The CBs were crosscut and offset by relatively low-angle shear bands of the second phase. Overprinting by joints and the evolution of joint-based strike-slip faults associated with Basin and Range extension followed [Eichhubl *et al.*, 2004; Flodin and Aydin, 2004a; Hill, 1989; Myers and Aydin, 2004; Sternlof *et al.*, 2004; Taylor *et al.*, 1999]. Noting their relative age and dominant orientation (north-northwest trend and steep dip), Hill [1989] first suggested that the CBs formed in response to east-northeast directed regional compression associated with tectonic shortening during the Cretaceous Sevier orogeny.

[5] Building on this earlier work, we present a conceptual and mechanical model of CBs in porous sandstone as anticrack inclusions [Sternlof and Pollard, 2001, 2002]. The particular utility of this hybrid interpretation lies in combining the analytical insights of Eshelby inclusion theory [Eshelby, 1957, 1959] with the power of boundary element method (BEM) simulations [Crouch and Starfield, 1983] to understand the mechanics of CB evolution. Starting with targeted field and petrographic observations of CBs

from the Aztec Sandstone in the Valley of Fire, we build a mechanical analysis of these structures as Eshelby-type inclusions to establish the validity and utility of a two-dimensional anticrack treatment of CBs using a displacement discontinuity BEM.

[6] The basic hypothesis underlying this research is that a fundamental mechanism of incremental, quasi-static and (anti)crack-like propagation was at work throughout the Aztec such that individual CBs tended to form orthogonal to the most compressive remote stress. The diversity of outcrop patterns observed therefore reflects the interactions of CBs with local material and stress heterogeneities through this fundamental propagation mechanism. Beyond contributing to the understanding of an interesting and generally overlooked mode of structural failure in porous, granular earth materials, this research is motivated by the practical goal of using mechanical understanding of the phenomenon to forecast its occurrence and associated fluid flow effects in active reservoirs and aquifers. Although the research presented here is built on detailed CB data acquired from a specific outcrop of Aztec Sandstone in the Valley of Fire, we suggest that the intrinsic attributes identified are common to all CBs in the Aztec and, by extension, to other



Figure 2. (left) Outcrop of widely spaced, relatively planar and parallel compaction bands along the northeast flank of Silica Dome. Arrows indicate opposite tips of a single band 62 m long and up to 15 mm thick (illusory gaps in band continuity are due to outcrop topography and breaks in the telltale fin). A total of 16 tip-to-tip thickness profiles were measured using a steel tape and calipers. (right) Illustration showing that even when closely spaced, compaction bands in this locale tend to remain planar (arrow indicates tip).

porous sandstones with similar depositional and tectonic histories.

2. Methods

[7] We focused on a “type locality” outcrop of CBs in Aztec Sandstone near Silica Dome in the Valley of Fire State Park (Figure 1, inset) where elementary patterns of approximately parallel bands are well exposed. Using a steel tape and calipers, we measured tip-to-tip thickness profiles of the two-dimensional band traces in outcrop (Figure 2), focusing on one example as representing the prototypical compaction band.

[8] Eleven cores were collected along the trace of one CB from tip to middle, as well as from essentially undisturbed sandstone nearby. These were vacuum-impregnated with optical-grade blue epoxy and used to make 37 standard and eight polished thin sections. Hue-based image analysis using MATLAB[®] was performed on more than 3500 color pictures taken from the standard sections with a digital camera mounted on a petrographic microscope. Intensity-based image analysis was performed on over 200 gray scale digital pictures collected with a scanning electron microscope (SEM). The particular SEM techniques used included backscatter electron imaging (BEI) and cathodoluminescence.

[9] The data acquired from the field and petrographic methods were used to inform three mechanical assessments

of the idealized anticrack inclusion conceptual model. Comparisons of the near-tip states of stress calculated with each of these continuum approaches constitute the heart of this paper, in which we use the convention of compression, closing mode displacement discontinuity and volume reduction strain as positive.

[10] The first approach considers the special case of an oblate ellipsoidal heterogeneity in the limit as its aspect ratio goes to zero, using the embedded-layer analysis of *Cocco and Rice* [2002] to construct algebraic expressions for the state of stress immediately ahead of the tip. The second approach employs an exact, closed-form solution to the general three-dimensional Eshelby problem [*Eshelby*, 1957, 1959; *Mura*, 1987] for the oblate ellipsoidal heterogeneity to calculate how the state of stress varies with distance from a model CB matching the idealized physical parameters of the field-based conceptual model. Finally, we turn to a numerical, two-dimensional BEM code in MATLAB to investigate the state of stress induced by an anticrack representation of the CB using only the trace length and effective closing mode displacement data.

3. Field and Petrographic Analysis

3.1. Geological Setting and Paleostress State

[11] The Aztec Sandstone, deposited during early to middle Jurassic time in a back arc basin setting, comprises the western edge of a continuous eolian system that

blanketed much of the intermountain southwest and includes the Navajo and Nugget sandstones [Blakey, 1989; Marzolf, 1983]. In the Valley of Fire area, the 1400-m-thick Aztec is directly and unconformably overlain by some 1300 m of Cretaceous sediments, which comprise a generally upward coarsening sequence of foreland basin deposits derived from Aztec highlands riding atop the two closest Sevier thrust sheets to the west. The smaller and easternmost of these, the Willow Tank thrust, placed lower Aztec on upper Aztec and as much as the first 600 m of Cretaceous deposits. The Willow Tank thrust sheet subsequently was overridden by the regionally extensive, kilometers-thick Muddy Mountain thrust, which placed Paleozoic carbonates over Aztec and provided the source for the upper Cretaceous units deposited atop the eastern reaches of the lower thrust sheet [Armstrong, 1968; Bohannon, 1983; Brock and Engleder, 1979; Carpenter and Carpenter, 1994; Longwell, 1949].

[12] Silica Dome is situated ~800 m above the bottom of the Aztec, at the lower end of the CB-rich upper half of the formation and just above a regional, subhorizontal alteration front separating uniformly red, hematite-stained sandstone below from bleached sandstone above [Taylor and Pollard, 2000]. The hematite staining is interpreted as syndepositional, while CBs are observed to be older than the bleaching front, which represents the lower extent of an alteration event attributed to the upward and eastward expulsion of reducing basinal brines by the advancing Muddy Mountain thrust sheet [Eichhubl et al., 2004]. This fluid flow event, along with at least one subsequent episode, is responsible for the vividly colorful patterns of iron mineralization for which the Valley of Fire is justly named. Eichhubl et al. [2004] cite a preponderance of evidence to argue that thrust emplacement stopped just west (Muddy Mountain thrust) and northwest (Willow Tank thrust) of more than 20 km² of Aztec outcrops, which now comprise the heart of the Valley of Fire and include the study area. They also present diagenetic evidence from the base of the Aztec indicating that it has never been buried much deeper than 3 km, a depth which matches the current combined thickness of Aztec and Cretaceous to lower Miocene deposits preserved in the area.

[13] Vertical loading of the Aztec during CB formation in the area thus appears to have been due solely to synorogenic deposition. A strong constraint on the upper limit of burial can be deduced from the relative timing of shear band formation. Everywhere they occur in the Aztec Sandstone, relatively low-angle shear bands of the second phase of deformation offset and thus postdate CBs [Flodin and Aydin, 2004b; Hill, 1989; Taylor and Pollard, 2000]. The dominant orientation and consistent top-to-the-east sense of shear displacement on these bands mimics that of the overlying Willow Tank thrust, suggesting a direct genetic relationship [Hill, 1989]. In fact, we observe that phase two shear bands extend into the Cretaceous deposits exposed directly beneath the thrust, while phase one CBs are confined to the Aztec Sandstone and all types of deformation bands are absent higher in the Cretaceous section. From these observations we infer that CB formation predated deposition of at least the upper 700 m of Cretaceous sediments.

[14] We conclude that the depth of Silica Dome at the time of CB formation ranged from 600 m (thickness of

overlying Aztec Sandstone) to 1200 m (Aztec plus up to 600 m of additional Cretaceous deposits). This corresponds to a range in vertical compressive stress from about 13 to 27 MPa, given an average overburden density of 2.25 g/cm³. Assuming that well-drained, near-surface water table conditions prevailed, as suggested by geologic, diagenetic, and paleoclimatic evidence [Eichhubl et al., 2004; Marzolf, 1983], pore pressure would have ranged from less than 6 MPa up to 12 MPa. Calculations based on Coulomb critical failure criteria [Zoback and Healy, 1984] and born out by a catalog of in situ stress measurements [Townend and Zoback, 2000] indicate that the ratio of maximum to minimum regional principal stress does not exceed about two under hydrostatic pore pressure conditions. Therefore, taking the Andersonian view [Anderson, 1951] that the minimum principal stress is vertical in thrust-faulting environments, both the maximum remote horizontal (tectonic) stress and the minimum horizontal stress could have ranged anywhere from 13 MPa up to 54 MPa.

[15] For the purposes of the mechanical analyses, we posit a “best estimate” paleostress state ($\sigma_1 > \sigma_2 > \sigma_3$) for Silica Dome of 40, 30, and 20 MPa. The value of σ_3 corresponds to an intermediate burial depth of 900 m (600 m of Aztec plus 300 m overlying Cretaceous deposits). The value of σ_1 corresponds to the implied limit of $2\sigma_3$ for active thrust fault environments, and is presumed to have acted parallel to the east vergent tectonic transport direction and perpendicular to the dominant northerly CB trend. The value of σ_2 is simply taken as the average of σ_1 and σ_3 . The mean (lithostatic) stress for this scenario is 30 MPa.

3.2. Outcrop Analysis

[16] Viewed individually at Silica Dome and elsewhere, CBs are seen to comprise sharply delineated tabular, bounded, and grossly penny-shaped structures that tend to weather out in positive relief as distinctive fins. They are generally between 1 cm and 2 cm thick in the middle and tens of meters in planar extent. Spacing between CBs ranges from centimeters to more than a meter (Figure 1). Truly isolated CBs are rare and close interactions between adjacent bands are common. Frequently though, as at Silica Dome, adjacent CB traces remain markedly straight and parallel even in close proximity (Figure 2). The appearance of CBs in outcrop, individually and in aggregate, is reminiscent of distributed opening-mode fractures, and CBs might easily be mistaken for veins or sand dikes by the casual observer. Closer inspection, however, reveals that they are composed of the same detrital material as the surrounding sandstone. In fact, depositional bedding is commonly preserved across the bands with no detectable shear offset (Figure 3).

[17] Sedimentary architecture in the Aztec is observed to affect CB distribution [Eichhubl et al., 2004; Hill, 1989; Sternlof et al., 2004]. Bands and patterns of bands frequently warp and/or terminate at or near cross-bed boundaries and almost always terminate at major interdune contacts. Also, while many if not most dune packages contain abundant CBs, some do not.

[18] Thickness profiles of 16 tip-to-tip individual CB traces ranging from one to 62 m long in outcrop reveal a characteristic, approximately elliptical shape (Figure 4a).

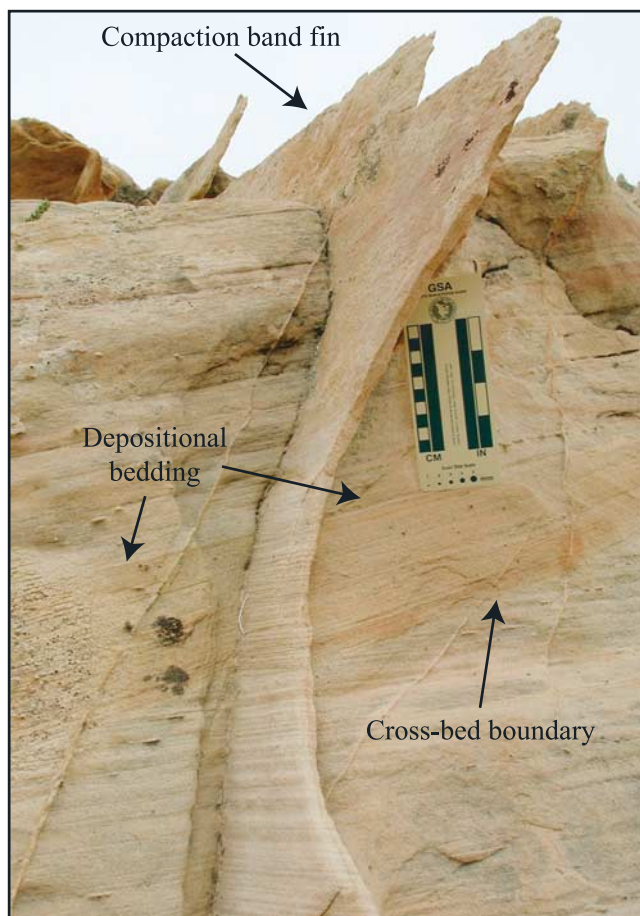


Figure 3. Close-up of a typical, well-developed compaction band fin in outcrop. Note that depositional bedding extends relatively undisturbed across the band and is clearly visible on the fin.

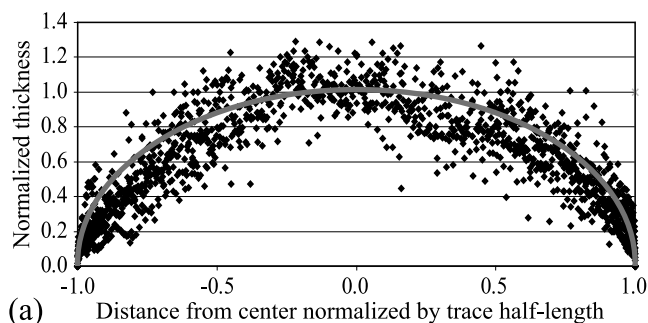
While midpoint thickness for these profiles generally increases with increasing trace length, it does so along a decreasing trend that suggests a plateau of maximum attainable thickness independent of trace length (Figure 4b). In order to capture the typical characteristics of a well-developed CB, we focused on one particularly isolated and symmetric outcrop trace of sufficient length and thickness that it could reasonably be assumed to represent a subhorizontal profile through the middle of the structure. This CB trace, designated CB-A (Figure 4c), is 24.75 m in length with a maximum midpoint thickness of 11.4 mm, yielding an aspect ratio (midpoint thickness/trace length) of 4.6×10^{-4} and an eccentricity of 0.99. Represented as an elliptical profile fit by the least squares method (correlation index 0.87), the midpoint thickness drops to 9.38 mm, thereby slightly decreasing the aspect ratio and increasing the eccentricity (Figure 4c).

[19] While this dimensional data was gathered on relatively low-angle outcrop faces, steep cliffs in the vicinity of Silica Dome and elsewhere in the Valley of Fire reveal that CBs can extend at least 10 m vertically. Coupled with the fact that they occur throughout a 700-m-thick section of the Aztec Sandstone, this observation supports what intuition suggests, that to first approximation CBs are

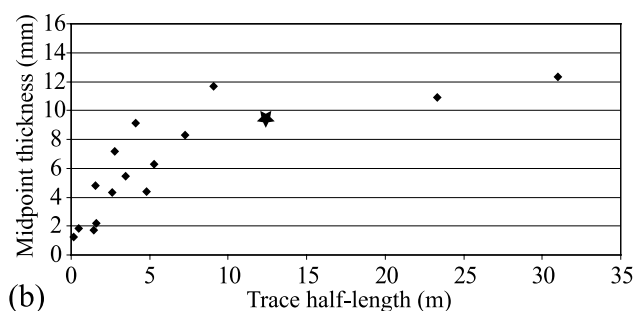
grossly penny shaped. Certainly, thickness is generally several orders of magnitude less than any in-plane, tip-to-tip dimension.

3.3. Petrographic Analysis

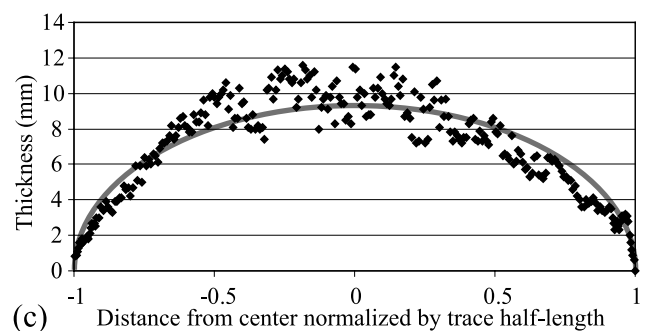
[20] Viewed in standard thin section, CB-A is every bit as sharply defined by its decreased porosity as it is in outcrop by its characteristic fin, and thickness measurements made under the microscope closely match those made with calipers in the field. Particularly striking is the absence of



(a) Thickness profile data for 16 tip-to-tip compaction band traces (>1700 measurements). Position is normalized relative to center by the band half length and thickness is normalized by the midpoint value. The curved line represents an ellipse similarly normalized. The correlation index of the data to the ellipse is 0.79.



(b) Plot of midpoint thickness versus trace half length for the 16 compaction band profiles, star indicates CB shown in Figure 4c. Thickness generally increases with increasing length, but along a decreasing trend.



(c) Thickness profile for CB-A, the 24.75-m-long compaction band trace featured in this paper. The curved line represents the least squares best fit of an ellipse to the data. The correlation index for this fit is 0.87.

Figure 4. (a) Thickness profile data for 16 tip-to-tip compaction band traces (>1700 measurements). Position is normalized relative to center by the band half length and thickness is normalized by the midpoint value. The curved line represents an ellipse similarly normalized. The correlation index of the data to the ellipse is 0.79. (b) Plot of midpoint thickness versus trace half length for the 16 compaction band profiles, star indicates CB shown in Figure 4c. Thickness generally increases with increasing length, but along a decreasing trend. (c) Thickness profile for CB-A, the 24.75-m-long compaction band trace featured in this paper. The curved line represents the least squares best fit of an ellipse to the data. The correlation index for this fit is 0.87.

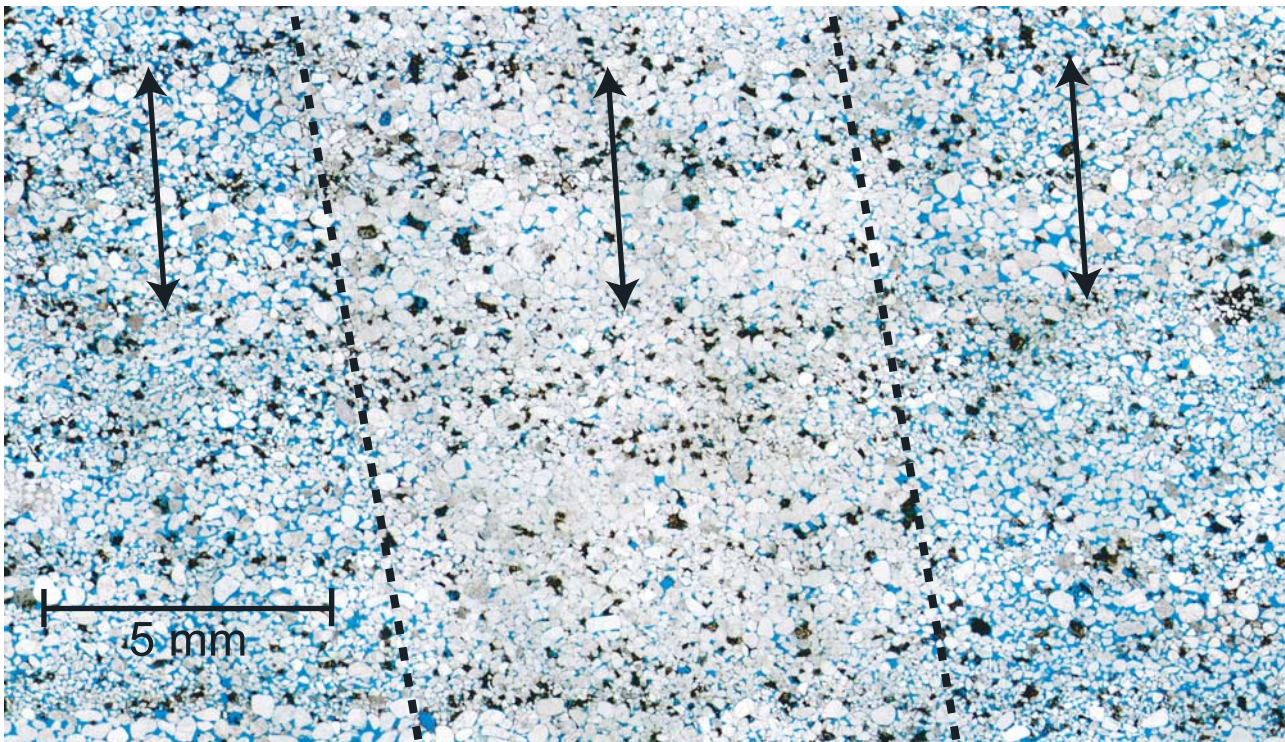


Figure 5. Photomicrograph of compaction band sampled 6.0 m from the tip, where it is ~ 9 mm thick (dotted black lines). Blue indicates epoxy-filled pore space ($\sim 25\%$ outside the band, $\sim 10\%$ inside). The plane of the section is vertical and orthogonal to the trace of the band in outcrop. This is a mosaic of images taken with plane-polarized transmitted light at 25X magnification using a digital camera mounted to a binocular microscope. Mineral constituents identifiable in this image are detrital quartz (white to gray), detrital orthoclase (stained dark brown), and sparse hematite (black). As is typical in foreset dune deposits, bedding generally consists of alternating layers of coarser and finer grains, here accentuated by the relative concentration of stained orthoclase in the finer-grained beds. Note that bedding is preserved, perhaps even visually enhanced within the band. The three black arrows indicate a coarse-fine-coarse bedding package as it passes through the band at high angle with no apparent change in thickness. The preservation of bed thickness is observed consistently in all thin sections, including those taken across the band and orthogonal to the orientation shown above at four locations. This indicates that compaction strain within the band is predominantly uniaxial and oriented parallel to the band-normal direction. Natural, millimeter-scale variations in bed thickness render more exact interpretations of bed distortion within the band inconclusive.

any well-developed structural fabric within the band, and the degree to which depositional bedding is preserved within and across it (Figure 5). In fact, nowhere did we find appreciable evidence of bedding offset across the band, despite considerable natural variability in the relative orientation of bedding to band between sample locations. Neither did we find any conclusive evidence of systematic bedding thickness variations within the band. Together these observations indicate that the inelastic strain accommodated within CB-A as porosity-loss compaction was predominantly uniaxial and directed parallel to its shortest dimension (i.e., perpendicular to its trace).

[21] Despite the coarseness inherent to porosity measurements, particularly using two-dimensional image analysis of granular materials, profiles across thicker parts of CB-A clearly reveal the abrupt drop in porosity that defines the band (Figure 6a). Mean porosity in the sandstone outside the band was measured to be 24.5%, with a standard deviation of 2.9%. Mean porosity inside the band was measured to be 11.9%, with a standard deviation of 3.0%.

Toward the tip, the profiles indicate the absence of any obvious near-tip process zone recognizable as spatial variations in porosity (Figure 6b).

[22] Backscatter electron images (BEI) provide much greater definition than the standard color digital images. In particular, microporosity due to grain damage can be distinguished and clay, which absorbs epoxy and so looks blue in standard sections, can be differentiated (Figure 7). The clay occurs primarily as undeformed grain-bridging and pore-filling cements, both inside and outside the CB. Clay also frequently infills cracked grains. These observations indicate that clay should be ignored when determining the distribution of porosity related to mechanical compaction. Image analysis reveals that the Aztec averages about 4% clay by volume, while thicker parts of the band and the sandstone immediately adjacent to it average about 7%. This preferential accumulation of pore-clogging clay, due presumably to groundwater filtering by the compacted band coupled with mechanically enhanced feldspar degradation, at least partially explains the greater resistance to

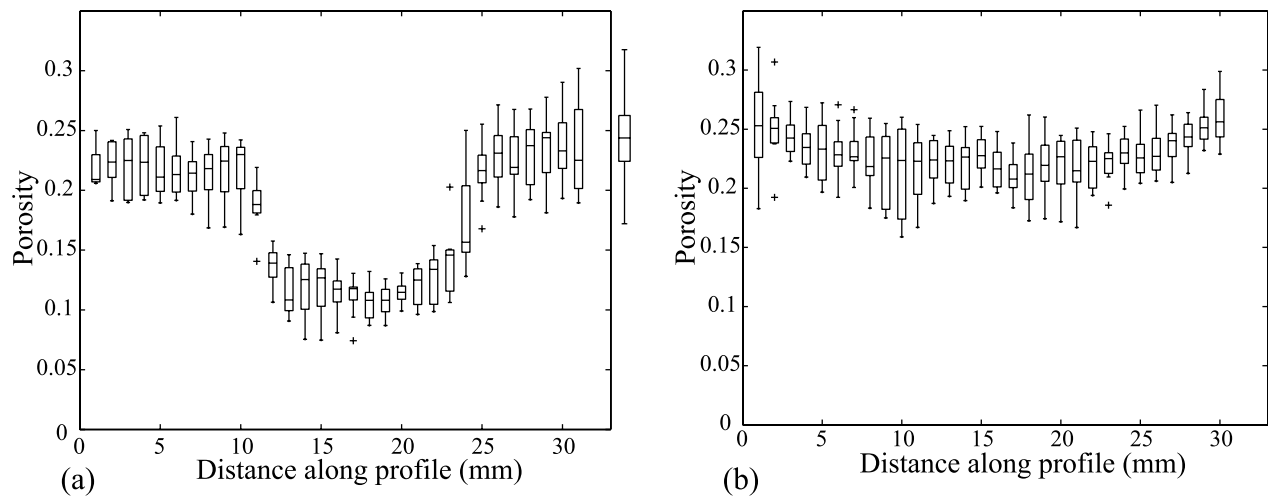


Figure 6. Porosity profiles taken orthogonally across the compaction band (a) 8.7 m from the tip and (b) at the tip. Each box plot represents a composite of 10 porosity measurements from immediately adjacent transects. The horizontal lines comprising the boxes indicate lower quartile, median and upper quartile values of the group. The whiskers extend up to 1.5 times the interquartile range to indicate the spread of additional data points. Outliers are indicated by crosses. A box plot representing the range of background matrix porosity (minus outliers) appears to the right of each profile. In Figure 6a, at its middle, the band is clearly defined as a sharp, statistically significant drop in porosity. In Figure 6b, at its tip, however, while still visually apparent at a fraction of a millimeter thick, the band can no longer be detected as a measurable reduction in porosity.

weathering exhibited by CBs, as well as their strong impact on fluid flow. That clay remains the primary cement in the weakly indurated Aztec today further suggests that cementation was light to nonexistent during CB formation.

[23] Six sets of backscatter images were collected at locations ranging from the middle to the tip of CB-A. Each set comprises images taken from inside and immediately outside the band within the same depositional layer(s). Porosity reduction volume loss related to CB formation at these locations ranged from 9.4% to 11.7% (Figure 8). These results suggest that mechanical compaction throughout the band is uniform at about 10%, regardless of the local variations in sandstone porosity through which it propagated. Cathodoluminescence imaging indicates that redistribution of quartz via pressure solution is volumetrically insignificant and has not appreciably contributed to the spatial distribution of porosity now observed. This is not surprising given the shallow burial history of the study area (<2 km), which, for any reasonable estimate of geothermal gradient, would have made quartz pressure solution an extremely slow to nonexistent process.

[24] Cracking of quartz grains at point contacts, due both to overburden and tectonic loading, is pervasive throughout the thin sections. Wholesale microfracture-accommodated plastic deformation of quartz grains, however, comprises the dominant microstructural characteristic of the band, and is the obvious mechanism by which granular rearrangement and porosity loss compaction was accommodated (Figure 9). Roughly half of the quartz grains within the band exhibit plasticity, creating the hint of a mild shape fabric of deformed grains elongated parallel to the band trace (i.e., orthogonal to the inferred

direction of maximum compression). Far more striking is the relative absence of granular disaggregation, despite often intense microfracturing and distortion. Taken together, these observations corroborate the field interpretation of the band as representing nearly pure uniaxial compaction with little or no shear, and suggest a stable, quasi-static process of plastic collapse.

[25] Isolated examples of grain plasticity and collapse can also be found outside the band (Figure 10). We interpret these as incipient CBs, representing an early stage of compaction around an original Griffith-type flaw (weak grain, irregular pore, etc.) which for any variety of reasons failed to develop further. Similar textural evidence of incipient grain damage and collapse immediately around the band and at the tip, however, is notably absent. Opening-mode fractures and faults typically exhibit a process zone of transitional deformation that grades into the surrounding undamaged host material, particularly around the tip where induced stress concentrations are highest [Hoagland *et al.*, 1973; Peck *et al.*, 1985]. Despite considerable effort, we have as yet been unable positively to identify any analogous process zone around the band, expressed either as grain damage or porosity variations.

4. Anticrack Inclusion Conceptual Model

[26] On the basis of the observations, data, and constraints presented above, we propose an idealized conceptual model of isolated compaction bands in porous sandstone as highly eccentric, roughly axisymmetric ellipsoidal features of sharply defined inelastic porosity-loss compaction, which form in response to and generally perpendicular with the maximum remote compressive tectonic stress (Figure 11a). We further suggest that CBs

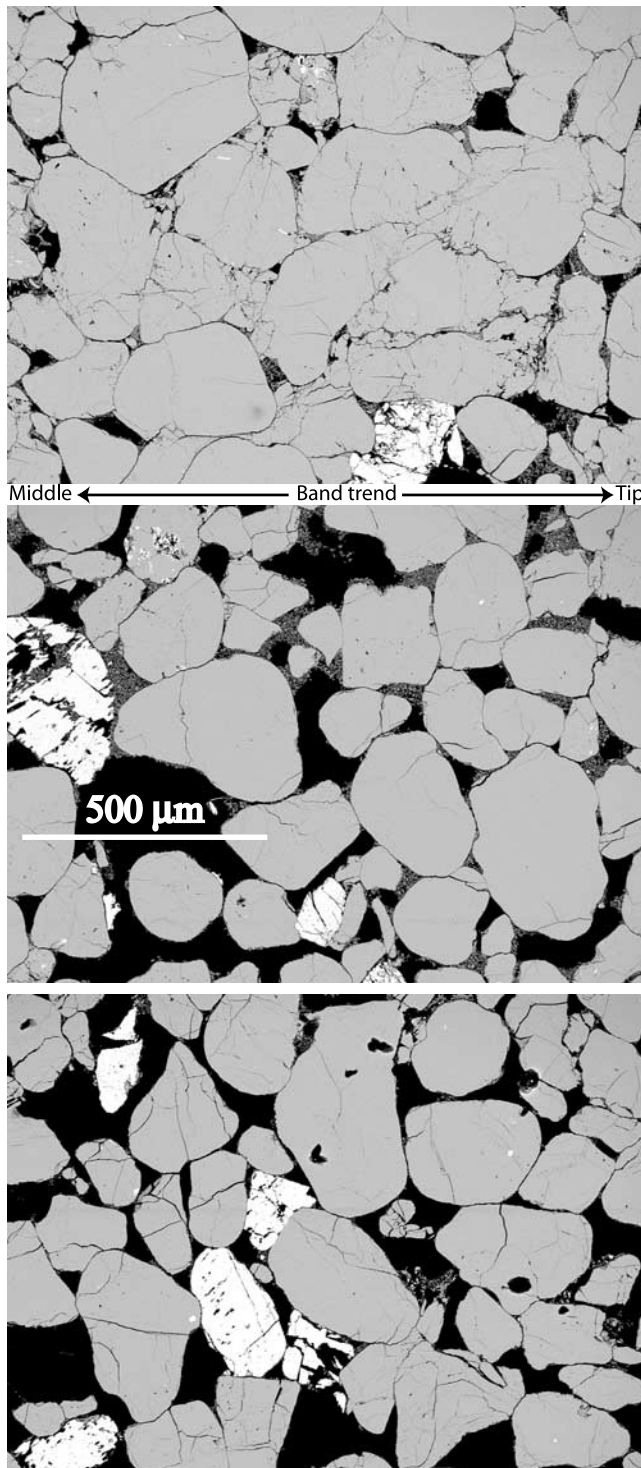


Figure 7. Compositional electron backscatter images of (top) a thick part of the compaction band, (middle) adjacent sandstone less than 2 mm outside the band, and (bottom) sandstone more than 1 m away from the nearest band. Porosity is black, quartz is medium gray, feldspar is white, and clay (kaolinite) shows as clusters of dark gray speckles around the detrital grains. Note the dominant texture of microfracture accommodated plasticity inside the compaction band versus the relative paucity of grain damage everywhere outside, even immediately adjacent to the band.

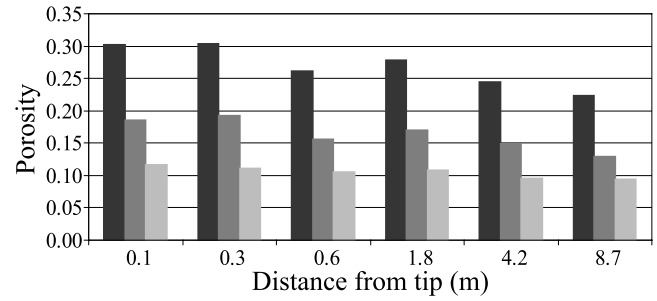


Figure 8. Clustered bar chart showing the variation of porosity inside (middle bar) and immediately outside (left bar) the compaction band as a function of distance from the tip (clay counted as porosity). The porosity change (right bar) represents the volume strain attributable to uniaxial compaction at each location. This compaction strain appears to be relatively uniform throughout the band at $\sim 10\%$.

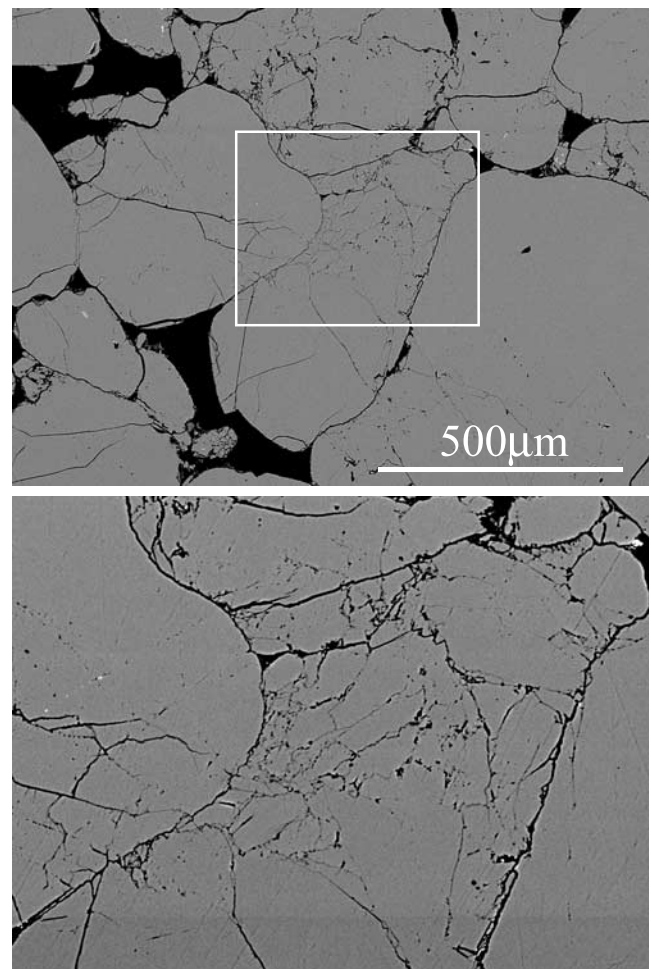


Figure 9. Electron backscatter images of microfracture-accommodated quartz grain plasticity and interpenetration, which comprises the dominant mode of grain-scale deformation inside the compaction band (white box in upper image indicates area of detail shown in lower image). Despite intense grain damage and the absence of appreciable quartz recrystallization, very little disaggregation of detrital grains is apparent.

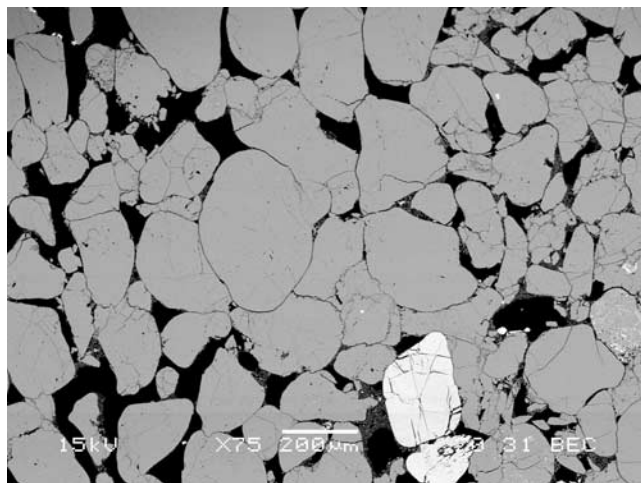


Figure 10. Compositional electron backscatter image of localized quartz grain plasticity and collapse (interlocked grains at center of image) that is not part of a well-developed compaction band. Similar grain-scale features appear scattered throughout the sandstone and can be interpreted as incipient compaction bands. Black is porosity, medium gray is quartz, and white is feldspar.

initiate with the collapse of Griffith-type grain-scale flaws (weak grains, irregular pores, etc.) and then propagate outward to form tabular inclusions of nearly uniform uniaxial plastic strain and differing elastic moduli embedded within a surrounding elastic medium. This conceptual model is well represented mechanically as a contractile Eshelby inclusion (Figure 11b), which would generate near-tip compressive stress concentrations in the surrounding material consistent with self-sustaining in-plane propagation. Inside any ellipsoidal inclusion embedded within an infinite medium, the state of stress and strain is uniform [Eshelby, 1957].

[27] The combination of extreme aspect ratio ($\sim 10^{-4}$) with significant uniaxial plastic strain (0.1) further suggests a close mechanical approximation of the idealized CB as an anticrack; that is, a sharp boundary across which a continuous distribution of closing mode displacement discontinuity has occurred (Figure 11c). This virtual anticrack interpretation for compaction bands is analogous to that of pressure solution surfaces [Fletcher and Pollard, 1981; Mollema and Antonellini, 1996], except that porosity loss takes the place of material dissolution and transport. In neither case does physical interpenetration occur, rather the boundary demarcating volume loss migrates outward and into the surrounding material.

[28] Central to the anticrack inclusion concept, and the mechanical analyses to follow, is the prescription of the model CB as an isolated feature of nonlinear inelastic strain that evolves quasi-statically in an infinite, homogeneous, isotropic, linear elastic continuum subject to uniform remote loading. All aspects of this model prescription warrant comment. First, given the regional tectonic nature of the compression and a study area situated in the midst of a 1400-m-thick sandstone deposit, the approximation of uniform remote stresses applied to an infinite material is reasonable. Given a ratio of trace length to spacing

generally less than 0.1, it would be difficult to argue that any CB in the Aztec Sandstone is truly isolated in a mechanical sense. Nonetheless, the specific field data on which the conceptual model is based comes from planar bands that betray little reaction to their nearest neighbors.

[29] As with any granular material, the applicability of homogeneous continuity is scale-dependent. In the Aztec Sandstone, with an average grain diameter of 0.25 mm, this becomes reasonable at the centimeter-scale [Amadei and Stephansson, 1997], which represents a lower limit of resolution for interpreting the mechanical modeling results. To focus on grain-scale processes inside and immediately

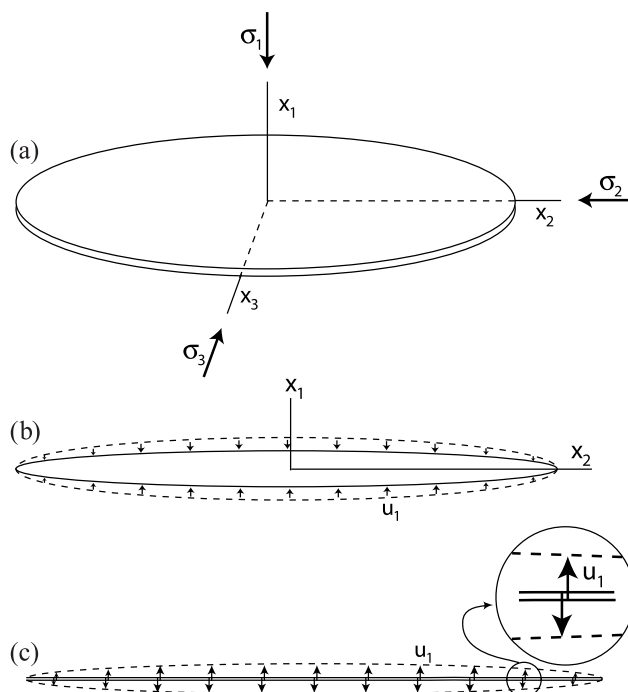


Figure 11. Schematic representations of the idealized compaction band model. (a) Axisymmetric geometry of the eccentric ellipsoidal band aligned with the principal remote stresses. (b) Cross-sectional area of the band (solid ellipse) relative to the precompact area originally occupied by the same detrital grains (dashed ellipse). As inelastic compaction progresses, the boundary around the grains involved contracts as indicated by the displacement arrows (u_1). This inward displacement of the elliptical boundary corresponds to the uniform uniaxial plastic strain of an Eshelby inclusion, and the area between the dashed and solid ellipses corresponds to the volume loss associated with the compaction. (c) Two-dimensional anticrack representation of the model band as an elliptical distribution of closing-mode displacement discontinuity equivalent to the uniform Eshelby compaction strain. In this virtual treatment, two material lines (solid lines) interpenetrate by an amount equivalent to the volume loss associated with the compaction (dashed ellipse) as shown by the displacement arrows (u_1). Actual interpenetration does not occur. Because of its extreme eccentricity, however, solutions for the state of stress induced around the model band using the Eshelby and anticrack approaches are substantially similar.

outside a CB, the distinct element method approach would be appropriate [Antonellini and Pollard, 1995; Morgan, 1999; Morgan and Boettcher, 1999]. Also problematic at a larger scale is the application of homogeneous isotropy to the complex eolian sedimentary architecture of the Aztec. Major dune boundaries influence CBs, so this conceptual model is based on data from an outcrop of bands located within a single dune package. Given that CBs commonly cut across depositional bedding without apparent effect, we interpret the mechanical influence of such layering as negligible. Finally, the assumption of quasi-static CB propagation is based on the coherent nature of plastic quartz grain deformation within the bands, which suggests stable propagation accommodated by slow, viscoelastic relaxation [Chester *et al.*, 2004; Karner *et al.*, 2003]. By the same token, the paucity of plastic deformation outside the bands suggests predominantly elastic behavior through time.

5. Elastic Properties

[30] Despite a long history of diagenesis and deformation, analysis of the Aztec Sandstone reveals a material arguably similar in terms of depositional structure and cementation to what it was during CB formation: a weakly cemented, cross-bedded, porous quartz sandstone. That autochthonous clay derived from the degradation of sparse feldspar has replaced thin hematite grain coatings as the primary cement is unlikely to have significantly altered the bulk material properties of the Aztec's close-packed quartz grain skeleton. We therefore infer that the elastic properties of the paleo-Aztec resemble those of the present day.

[31] Published values for apparent Young's modulus in sandstones based on laboratory testing range from 10 to 46 GPa (mean of 22 GPa), while apparent Poisson's ratio ranges from 0.1 to 0.4 (mean of 0.24) [Bieniawski, 1984]. We have calculated values of apparent Young's modulus for samples collected near Silica Dome from the results of triaxial compression tests conducted at Sandia National Laboratories. The results were 16.5 and 21.0 GPa at confining pressures of 10 and 50 MPa, respectively. Given the assumed lithostatic paleostress of 30 MPa, we therefore posit a Young's modulus of 20 GPa and a Poisson's ratio of 0.2 for the Aztec Sandstone at Silica Dome during the period of CB formation.

[32] The CBs themselves, however, are a different matter. Preferential clay cementation of the bands subsequent to their formation has rendered them significantly more resistant and, presumably, stiffer than the friable host rock. Indeed, induration of the bands can occasionally resemble that of quartzite, suggesting that local pressure solution healing of damaged grains may have occurred. Even if the current elastic properties of CBs could reliably be measured in the lab, a difficult challenge given their thin, tabular dimensions, we suggest that the results would not represent the bands as they formed. Additionally, the texture of the bands presents a paradox in that reduced porosity argues for increased shear stiffness, while intense microfracturing and effective grain size reduction argues for increased shear compliance. It is reasonable to assume, however, that bulk modulus within CBs, which measures resistance to volume change, would increase as the result

of both porosity loss and effective grain size reduction. In the analyses that follow, we therefore consider a range of elastic properties for the model CB by fixing the ratio of band to sandstone bulk moduli at 1.5. The interrelation of the essential elastic parameters (Young's modulus (E), shear modulus (G), bulk modulus (K) and Poisson's ratio (ν)) is given by $E = 2G(1 + \nu) = 3K(1 - 2\nu)$.

6. Mechanical Analysis

[33] A logical minimum requirement for in-plane propagation of the model CB is that compressive stress just ahead of the tip, whether the component normal to the band trace, the mean value, or some other measure, exceeds the remote value. If the compacted material inside the band becomes elastically stiffer than the surroundings, the compressive stress at the tip will decrease. If the inside is softer, the compressive stress will increase. The other critical independent factor is the magnitude of the inelastic strain represented by the compaction, which would act to increase the magnitude of the near-tip compressive stress.

[34] In this section, we first use an embedded-layer model to develop these ideas in a quantitatively intuitive way, examining the relative influence of elastic moduli versus inelastic strain on the state of stress exactly at the tip of an infinitely thin band. We then turn to a full analytical solution of the Eshelby problem to examine the state of stress induced around a band matching the parameters of the field-based conceptual model. Finally, we compare the results obtained with the Eshelby solution to those derived from a two-dimensional (plane strain) BEM approximation of the model band as an anticrack, using a distribution of closing mode displacement discontinuity elements to represent the 10% homogeneous uniaxial strain of the inclusion.

6.1. Embedded Layer Model

[35] Expressions for the stress and strain fields in and around an Eshelby inclusion are given by Rudnicki [1999] in terms of the remote values, the elastic constants of the inclusion and surrounding material, and an array of factors depending on the geometry of the inclusion and the Poisson's ratio of the surroundings. He specifically treats the limiting case of interest here, where the aspect ratio of the inclusion goes to zero and its geometry approaches that of an embedded layer. The same result can be obtained more directly from the conditions given by Cocco and Rice [2002] for a planar fault zone. Comparison of the two approaches establishes the formal equivalence of the very eccentric ellipsoidal inclusion with the embedded layer.

[36] With the x_1 axis normal to the layer and parallel to the short axis of the inclusion (Figure 11a), Cocco and Rice [2002] note that $\epsilon_{ij}^b = \epsilon_{ij}^\infty$ if neither i nor j is 1 and $\sigma_{ij}^b = \sigma_{ij}^\infty$ if either i or j is 1, where the superscripts "b" and " ∞ " denote values of stress (σ) and strain (ϵ) inside the model band (layer/inclusion) and in the far field, respectively. The relations of particular relevance here are

$$\sigma_{11}^b = \sigma_{11}^\infty \quad (1a)$$

$$\epsilon_{22}^b = \epsilon_{22}^\infty, \epsilon_{33}^b = \epsilon_{33}^\infty \quad (1b)$$

Hooke's law for the linear elastic relation between strain and stress is

$$\varepsilon_{ij} = \frac{1}{2G} \left\{ \sigma_{ij} - \frac{\nu}{1+\nu} \sigma_{kk} \delta_{ij} \right\} \quad (2)$$

where the repeated index denotes summation, and $\delta_{ij} = 1$ if $i = j$, and 0 if $i \neq j$. The remote stresses and strains are related by (2). In the band, (2) relates the stresses to the elastic strains. The total strain inside the band is given by

$$\left[\varepsilon_{ij}^b \right]^{\text{total}} = \left[\varepsilon_{ij}^b \right]^{\text{elastic}} + \varepsilon_{ij}^p \quad (3)$$

where ε_{ij}^p denotes the plastic strain representing compaction within the band, which equals zero unless $i = j = 1$ as stipulated in the field-based conceptual model. Equations (1), (2), and (3) can be combined to eliminate the elastic strains and yield expressions for the stresses inside the model band in terms of the far-field stresses and elastic constants:

$$\sigma_{11}^b = \sigma_{11}^\infty \quad (4a)$$

$$\sigma_{22}^b = \frac{1+\nu_b}{2(1-\nu_b)} \left\{ \frac{(1-\nu_s)G_b}{(1+\nu_s)G_s} (\sigma_{22}^\infty + \sigma_{33}^\infty) + \sigma_{11}^\infty \cdot \left[\frac{2\nu_b}{(1+\nu_b)} - \frac{G_b}{G_s} \frac{2\nu_s}{(1+\nu_s)} \right] \right\} + \frac{G_b}{G_s} \frac{(\sigma_{22}^\infty - \sigma_{33}^\infty)}{2} \quad (4b)$$

$$\sigma_{33}^b = \frac{1+\nu_b}{2(1-\nu_b)} \left\{ \frac{(1-\nu_s)G_b}{(1+\nu_s)G_s} (\sigma_{22}^\infty + \sigma_{33}^\infty) + \sigma_{11}^\infty \cdot \left[\frac{2\nu_b}{(1+\nu_b)} - \frac{G_b}{G_s} \frac{2\nu_s}{(1+\nu_s)} \right] \right\} - \frac{G_b}{G_s} \frac{(\sigma_{22}^\infty - \sigma_{33}^\infty)}{2} \quad (4c)$$

where the subscripts "b" and "s" denote the elastic parameters of the band and surrounding sandstone, respectively.

[37] The state of stress at the point adjacent to and immediately outside the tip of the model band along the x_2 axis can now be obtained from the conditions of displacement and traction continuity at the interface:

$$\sigma_{22}^t = \sigma_{22}^b \quad (5a)$$

$$\varepsilon_{11}^t = \varepsilon_{11}^b, \quad \varepsilon_{33}^t = \varepsilon_{33}^b \quad (5b)$$

where the superscript "t" refers to the values just outside the tip. In the second equation of (5b), ε_{33}^t can be replaced by ε_{33}^∞ from the second equation of (1b). Again, the elasticity relations can be used to eliminate the elastic strains and yield expressions for the stresses at the tip of the band in terms of the uniform stresses inside, the elastic constants and the nonzero plastic strain component ε_{11}^p :

$$\sigma_{11}^t = \frac{G_s}{G_b} \sigma_{11}^b + \frac{\nu_s}{(1-\nu_s)} \sigma_{22}^b \left(1 - \frac{G_s}{G_b} \right) + \frac{G_s}{G_b} \sigma_{kk}^b \frac{\nu_s - \nu_b}{(1-\nu_s)(1+\nu_b)} + \frac{2G_s}{(1-\nu_s)} \varepsilon_{11}^p \quad (6a)$$

$$\sigma_{22}^t = \sigma_{22}^b \quad (6b)$$

$$\sigma_{33}^t = \frac{G_s}{G_b} \sigma_{33}^b + \frac{\nu_s}{(1-\nu_s)} \sigma_{22}^b \left(1 - \frac{G_s}{G_b} \right) + \frac{G_s}{G_b} \sigma_{kk}^b \frac{\nu_s - \nu_b}{(1-\nu_s)(1+\nu_b)} + \frac{2G_s}{(1-\nu_s)} \nu_s \varepsilon_{11}^p \quad (6c)$$

[38] By substituting (4) into (6), expressions for the stresses at the tip in terms of the remote values also can be derived. It can be seen from (6) that for given values of the elastic parameters and remote stresses, σ_{11}^t and σ_{33}^t are linear functions of ε_{11}^p , with slopes of $2G_s/(1-\nu_s)$ and $[2G_s/(1-\nu_s)]\nu_s$, respectively, while σ_{22}^t remains constant. In fact, for $\varepsilon_{11}^p > 10^{-3}$ and any realistic range of elastic parameters and remote stresses, the final term in (6a) and (6c) begins to dominate the tip stress state, with σ_{11}^t increasing linearly with ε_{11}^p at a rate $1/\nu^\infty$ times greater than σ_{33}^t .

[39] Figure 12 illustrates this relationship using the putative remote stress state and elastic parameters defined above. Normal stress components at the tip are plotted as functions of ε_{11}^p from 0 to 0.1 for two cases: $G_b = 2.182G_s$ and $\nu_b = 0.5\nu_s$ (solid lines), and $G_b = 0.857G_s$ and $\nu_b = 2\nu_s$ (dotted lines). Thus $E_b = 2E_s$ in the first case and $0.5E_s$ in the second, while in both cases, $K_b/K_s = 1.5$. The two sets of lines lie virtually on top of each other over the entire range of ε_{11}^p , indicating not only that the actual plastic strain of 0.1 dominates the state of stress at the tip, but that the elastic properties inside the model band have a negligible effect on the state of stress even as ε_{11}^p approaches zero.

[40] The results of this analysis, however, pertain only to a point infinitesimally close to the tip of an infinitesimally thin ellipsoidal inclusion. The aspect ratio of the idealized ellipsoidal CB is small (10^{-4}) but not zero, and the approximation of the granular Aztec Sandstone as a homogeneous continuum makes looking very close to the tip problematic. We therefore turn to a complete analytical solution of the Eshelby problem to match the exact physical parameters of the field-based conceptual model and extend the analysis away from the band-sandstone interface.

6.2. Eshelby Inclusion Model

[41] For this analysis, we use an exact, closed form solution to the general three-dimensional Eshelby problem based on the equivalent inclusion method. The solution is coded in MATLAB and was made available to us by P. Sharma at the University of Houston. Within certain limitations, the code accepts any combination of ellipsoidal inclusion dimensions, internal and external elastic properties and remote loading to calculate the state of stress for any point outside the inclusion. The embedded-layer stress results in Figure 12 can be reproduced to within a fraction of 1% using the Eshelby code, by inputting an axisymmetric inclusion with a 10^{-7} aspect ratio and calculating the state of stress just outside (within machine precision) of the tip.

[42] To represent the field-based conceptual model, dimensions of 25 m by 25.1 m by 9.38 mm are used, along with a fixed value of $\varepsilon_{11}^p = 0.1$. The orientation of the model band with respect to the remote stress field, the range of elastic parameters inside and outside the band, and the magnitudes of the remote stresses remain the same as in

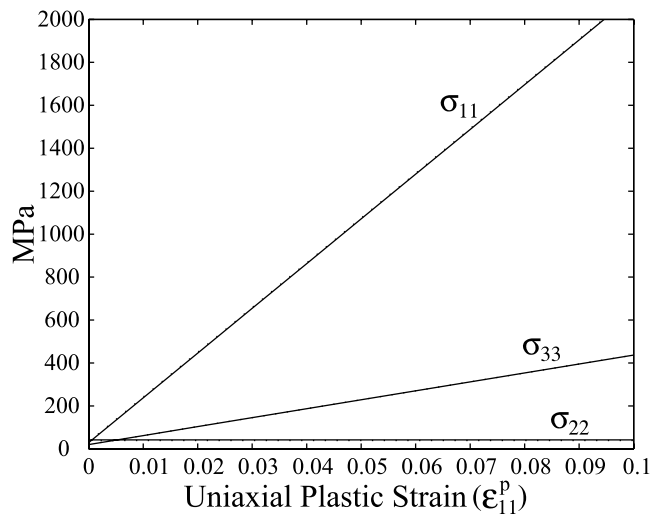


Figure 12. Components of normal stress just outside the tip of the model compaction band as linear functions of the uniaxial plastic strain from the embedded-layer solution. Two scenarios are plotted: one for a band with Young's modulus twice that of the surrounding material (solid lines) and one with Young's modulus half that of the surroundings (dotted lines). In both cases, the band/surroundings ratio of bulk moduli is 1.5, and the lines plot virtually on top of each other. The state of stress at the tip is dominated by the plastic strain and insensitive to differences in elastic properties.

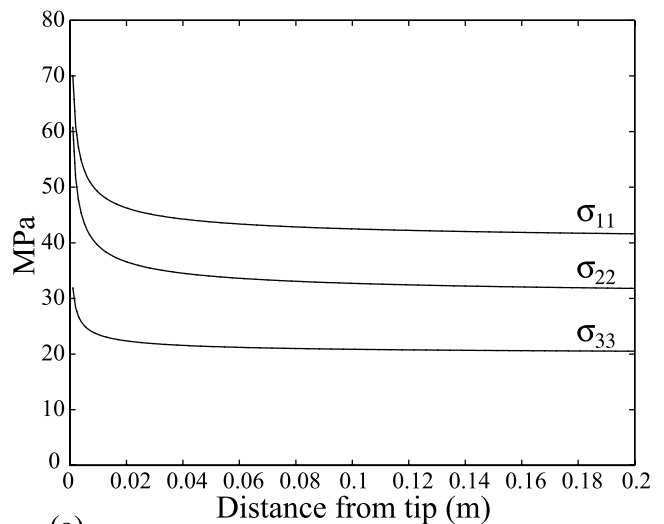
the embedded-layer analysis. Figure 13 presents the resulting stress distributions outside the model band away from the tip along the x_2 axis (Figure 13a) and away from the midpoint of the flank along the x_1 axis (Figure 13b). Once again, there is a negligible difference between the results obtained over a realistic range of shear stiffness contrast between the band and surrounding material for K_b/K_s fixed at 1.5. At about one mm from the tip, the compressive normal stresses are about double their remote values. This stress concentration dies away rapidly with distance, dropping to about 1.25 times the remote values at one cm from the tip, and decaying to a residual increase of about 5% within 20 cm. Immediately adjacent to the flank of the band, the compressive normal stresses drop by less than 3% relative to the remote values, and then smoothly rebound to effective background levels within about 10 m (σ_{22} and σ_{33}) and 20 m (σ_{11}).

[43] This Eshelby formulation provides the most accurate possible representation of the field-based conceptual model, and the results reinforce the conclusion from the embedded-layer analysis that the perturbed state of stress induced is overwhelmingly a function of the plastic strain accommodated. Even allowing the relative bulk modulus within the model band to vary outside realistic bounds, from volumetrically very compliant ($K = 4.2$ GPa) to very stiff ($K = 66.7$ GPa), exerts a negligible effect on the resulting near-tip stress field when $\varepsilon_{11}^p = 0.1$. Departures from the prescribed axisymmetric geometry also yield minimal effect. Holding the x_2 dimension of the model band constant at 25 m and varying the x_3 dimension from 6.25 m ($1/4x_2$) to 100 m ($4x_2$) produces a variation of less

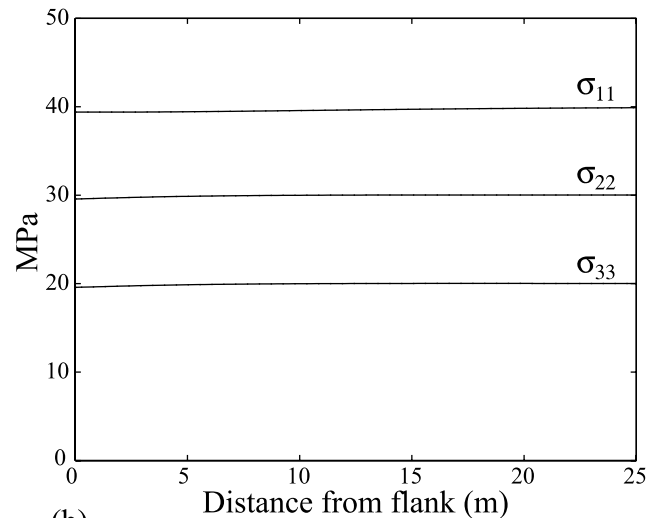
than 5% in the magnitude of σ_{33} realized one cm in front of the tip.

6.3. Anticrack Model

[44] The preceding analyses indicate the primary importance of the uniaxial plastic strain accommodated within an idealized CB in determining the state of stress induced around it. This suggests that an anticrack treatment of the problem, with a specified distribution of closing mode displacement discontinuity taking the place of internal



(a)



(b)

Figure 13. Distributions of the components of norm stress with distance from the model compaction band (a) tip and (b) flank, as calculated using the Eshelby inclusion solution and uniform uniaxial strain of 10%. Two scenarios are plotted: one for a band with Young's modulus twice that of the surrounding material (solid lines) and one with Young's modulus half that of the surroundings (dotted lines). For both scenarios the band/surroundings ratio of bulk moduli is 1.5 and, at both tip and flank, the lines plot virtually on top of each other. The state of stress is insensitive to differences in elastic properties and only significantly perturbed within a few centimeters of the tip.

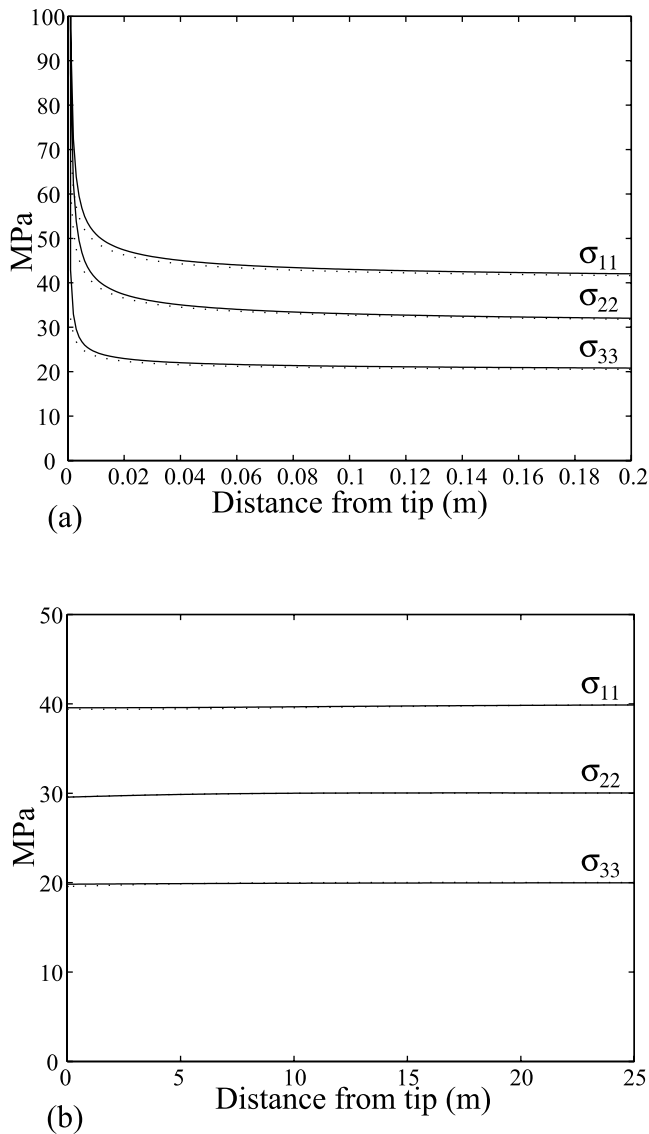


Figure 14. Distributions of the components of normal stress with distance from the model compaction band (a) tip and (b) flank, as calculated using the BEM anticrack solution (solid lines) and Eshelby inclusion solution (dotted lines). Beyond 2 cm from the tip, the two solutions agree to within 1%. They increasingly diverge as the anticrack solution goes toward infinity at the tip, while the Eshelby solution remains finite. Adjacent to the flank, differences between the two solutions are less than 1% everywhere.

plastic strain, would also capture the essential mechanical nature of the conceptual model. To test the validity of this proposition, we turn to a simple, two-dimensional displacement discontinuity representation of the idealized CB as an anticrack [Sternlof and Pollard, 2002] and use a BEM approach [Crouch, 1976; Crouch and Starfield, 1983] coded in MATLAB to solve it.

[45] In this analysis, we consider the principal $x_1 - x_2$ (horizontal) plane through the middle of the CB, which roughly corresponds to the outcrop face from which the field data were collected. The 25-m-long CB trace is

represented by 2500-cm-long constant displacement discontinuity boundary elements laid end-to-end along the x_2 axis from -12.5 m to $+12.5$ m. The closing mode displacement discontinuity of each element is calculated from the elliptical relation

$$D_i = \left(\frac{T_{\max}}{0.9} - T_{\max} \right) \sqrt{1 - \left(\frac{x_i}{a} \right)^2} \quad (7)$$

where D_i is the closing mode displacement discontinuity of the i th element, T_{\max} is the maximum (midpoint) thickness of the CB trace (9.38 mm), x_i is the x_2 coordinate of the midpoint of the i th element, and a is the half length of the trace (12.5 m). This yields a stepwise distribution of closing mode displacement discontinuity equivalent to the homogeneous uniaxial plastic strain of 10% used above. Because displacement is specified, the elastic properties of the CB do not enter the formulation. Also, the assumption of plane strain dictates that at every point in the $x_1 - x_2$ plane, $\sigma_{33} = \nu_b(\sigma_{11} + \sigma_{22})$ and $\sigma_{13} = \sigma_{23} = 0$.

[46] Figure 14 shows the resulting anticrack distribution of normal stresses away from the tip along the x_2 axis, and away from the flank along the x_1 axis as compared to those computed with the Eshelby model. Within one mm of the tip, where the singularity of the anticrack solution produces stresses tending toward infinity, correspondence is poor (Figure 14a). At 1 cm, the two solutions correspond to within 5% for all normal stress components. Beyond 2 cm the mismatch drops to less than 1%, with the anticrack values always slightly above the Eshelby values. At the flank, correspondence between the two solutions is excel-

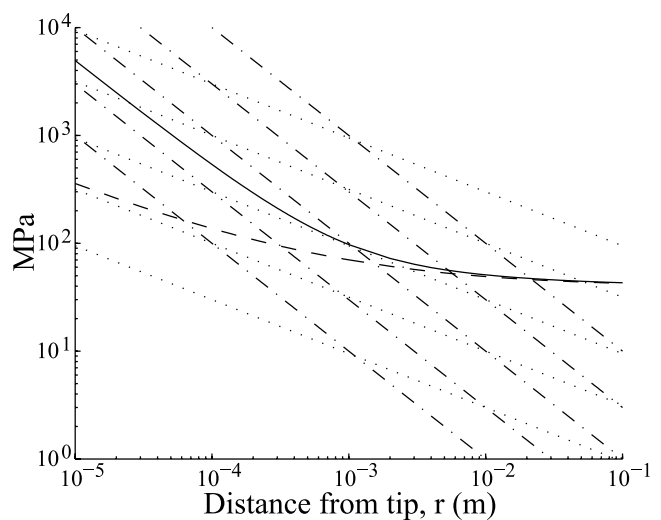


Figure 15. Log-log plot of the distribution of σ_{11} with distance from the model compaction band tip: BEM anticrack solution (solid line), Eshelby inclusion solution (dashed line), crack-like contours of $1/\sqrt{r}$ (dotted lines), dislocation-like contours of $1/r$ (dash-dotted lines). At the distance $r = 1$ cm from the tip, the two solutions effectively coincide. As r decreases, the Eshelby solution approaches the $1/\sqrt{r}$ distribution, although it remains finite. The BEM anticrack solution, which is composed of a stepwise distribution of constant closing mode displacement discontinuity elements, goes to infinity as $1/r$.

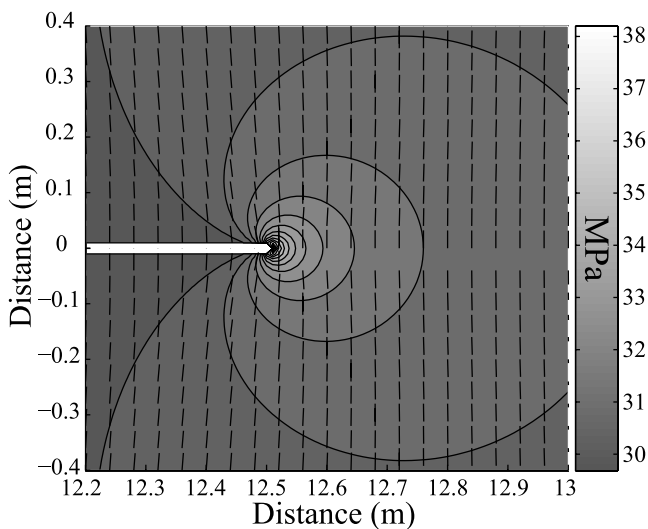


Figure 16. Contour plot of mean normal stress at the tip of the model anticrack compaction band (band represented by white slot). The remote mean normal stress is 30 MPa. Tick marks indicate the local orientation of the maximum principal stress.

lent, with less than a 1% mismatch for all normal stress components at any distance (Figure 14b).

[47] Figure 15 highlights the correspondence between the near-tip distributions of σ_{11} for the anticrack and Eshelby models on a log-log plot. Within a distance (r) from the tip of less than 0.2 mm, the anticrack distribution of σ_{11} is dominated by the constant displacement (dislocation) tip element, varying roughly as $1/r$ [Weertman and Weertman, 1964]. For distances greater than 0.2 mm and less than about 2 mm, the anticrack distribution varies roughly as $1/\sqrt{r}$, as expected for a true crack solution [Lawn, 1993]. For distances greater than 2 mm, the magnitude of σ_{11} decreases more gradually toward the remote value of 40 MPa. The Eshelby distribution of σ_{11} , on the other hand, varies much more gradually with distance from the tip, only beginning to approach $1/\sqrt{r}$ inside about 0.01 mm. Beyond 1 cm from the tip, the anticrack and Eshelby distributions of σ_{11} effectively coincide.

[48] The size, shape, and magnitude of the stress perturbation generated at the tip of the model anticrack CB is entirely consistent with the field-based interpretation of self-sustaining in-plane propagation oriented generally orthogonal to the maximum remote principal stress. For example, elevated mean normal (lithostatic) stress, which would tend to favor compaction, is tightly concentrated immediately in front of the tip, while the maximum local principal stress acts everywhere nearly perpendicular to the trace of the existing band (Figure 16).

7. Discussion

[49] The results presented above demonstrate the efficacy of the two-dimensional, numerical BEM anticrack approach in representing the full three-dimensional Eshelby state of stress generated around an idealized CB. The only significant mismatch occurs within one cm of the tip, which in any case is the length scale at which the model prescription

of homogeneous material continuity begins to depart from the granular reality of the Aztec Sandstone. We argue therefore that the anticrack formulation is both sufficient and even preferable for the purposes of modeling CBs from two-dimensional outcrop data. Other advantages include increased computational efficiency, the ability to handle asymmetric configurations of multiple CBs with nonuniform distributions of closing mode displacement (i.e., plastic strain), and the potential for modeling active propagation and pattern development at the outcrop scale [Sternlof *et al.*, 2003].

[50] This study also highlights several interrelated and enigmatic issues that warrant further investigation: the apparent absence of a near-tip end zone expressed either as variations in porosity or concentrated grain damage; the observation that thickness profiles of isolated CBs are elliptical for meters to tens of meters from the tip; the marked concentration of quartz plasticity within the bands and the spatial uniformity of the plastic strain thereby accommodated; and the apparent distribution of perturbed compressive stress that suggests grain damage could only occur within a few cm of the tip.

[51] Ultimately, we anticipate that more refined microscopic examinations will reveal the presence of a near tip CB process zone defined by quartz grain damage and incipient plasticity, and that the diameter of this softened damage zone may correlate to a maximum attainable band thickness independent of trace length. Certainly, most of the uniform inelastic compaction accommodated within a CB occurs well behind the tip line in an environment of reduced compressive stress that would seem to preclude thickening of the band by lateral propagation into undamaged sandstone. We suggest that the characteristically elliptical profile of an isolated band could be due primarily to relatively rapid mechanical propagation of the tip line, compared to relatively slow processes of plastic collapse and progressive thickening within the rind of damaged grains left in its wake.

[52] In terms of the bulk material and stress-strain conditions conducive to compaction localization in sandstone, as well as the mechanical characteristics of the phenomenon, this analysis of natural CBs in the Aztec Sandstone presents a scenario seemingly at odds with results and interpretations reported in the recent experimental and theoretical rock mechanics literature. First, regarding material and load conditions, we understand the phenomenon to have occurred in well-consolidated, saturated, but essentially uncemented sandstone at moderate mean compressive stresses consistent with burial of less than 2.5 km in a thrust-faulting tectonic regime. Laboratory efforts to induce compaction localization in triaxial experiments have tended to focus on moderately to well-cemented sandstones (e.g., Berea, Bentheim and Castlegate) generally subjected to much greater confining pressures reaching as high as 300 MPa [e.g., Wong *et al.*, 2001], which is equivalent to more than 12 km of overburden and enough to induce brittle-ductile transition behavior. The grain-scale textures of compaction resulting from such experiments also tend to involve intense grain crushing and comminution far in excess of that observed in natural CBs.

[53] Second, the mechanical style of compaction induced in the laboratory differs fundamentally from that observed

in the field, where discrete CBs appear to have initiated throughout the upper Aztec at widely distributed flaws, and then propagated outward along their tip lines to form a pervasive fabric grossly symmetric to the maximum remote compressive stress. The typical experiment, on the other hand, has produced a compaction front of damage that propagates across the specimen from one end cap toward the other, traveling in the direction of maximum compression and leaving fully compacted material in its wake [e.g., Baud et al., 2004; Olsson and Holcomb, 2000]. Such results have been convincingly interpreted in theoretical terms as a stress/strain bifurcation from homogeneous to localized compaction [Issen and Rudnicki, 2000, 2001; Olsson, 1999].

[54] We suggest, however, that this snowplow-like progression of compaction is an experimental phenomenon largely unrelated to natural compaction localization as observed in the Aztec Sandstone at the Valley of Fire. Similarly, the practical applicability of bifurcation analysis is somewhat limited both by the stipulation of initial stress/inelastic strain homogeneity, and by the fact that it applies only to the moment of localization without reference to any geometric constraint other than imposed planarity. By contrast, the observations and analysis reported in this paper indicate that compaction localization in the Aztec nucleated around grain-scale material heterogeneities acting as Griffith stress concentrators, and that the subsequent evolution of realistic CB arrays can be understood as the simultaneous propagation and interaction of many discrete bands modeled as anticracks.

[55] Despite the temporal and physical limitations inherent to experimental modeling, we therefore suggest that a key to progress in compaction localization research lies in introducing stress-concentrating initial flaws to jumpstart the deformation process in more representative materials subjected to less extreme loading conditions. The rate and state effects of pore water [Baud et al., 2000] and heat [Chester et al., 2004] might also catalyze improved results at laboratory scales and strain rates. A handful of recent experiments have incorporated the initial flaw idea [Sternlof and Pollard, 2002] as a circumferential notch designed to concentrate the applied load and localize compaction away from the end caps [Tembe et al., 2005; Vajdova and Wong, 2003]. Although still conducted on well-cemented sandstones subjected to unrealistically high confining pressures, these experiments have produced some promising results. Another set of experiments, although originally designed to investigate borehole breakouts in sandstone, have produced perhaps the most representative CBs yet achieved in the laboratory [Haimson, 2003; Haimson and Lee, 2004].

[56] **Acknowledgments.** Our thanks to John Childs (Figure 1) and Frantz Maerten for their able assistance in the field and to the Valley of Fire State Park staff and Superintendent Jim Hammons for access, support, and permission to collect samples. We also are deeply indebted to Gaurav Chopra, Pradeep Sharma, and Ole Kaven for their computational and coding work using MATLAB[®]. Chopra developed the BEM code used in this paper, while Sharma graciously provided the Eshelby code, which was modified for our use by Kaven. Tapan Mukerji provided invaluable assistance on issues of image analysis and rock physics, while Bob Jones enabled the SEM effort. Dave Lockner (U.S. Geological Survey), and Bill Olsson and David Holcomb (Sandia National Laboratories) graciously allowed us to conduct preliminary testing of our ideas in the lab, while providing many useful insights. This work was funded under grants from the U.S. Department of Energy, Office of Basic Energy Science, Geo-

sciences Research Program to John Rudnicki (DE-FG02-93ER14344) and David Pollard (DE-FG03-94ER14462), with additional support from the Stanford Rock Fracture Project.

References

- Amadei, B., and O. Stephansson (1997), *Rock Stress and its Measurement*, 490 pp., CRC Press, Boca Raton, Fla.
- Anderson, E. M. (1951), *The Dynamics of Faulting and Dyke Formation With Application to Britain*, 206 pp., Oliver and Boyd., White Plains, N. Y.
- Antonellini, M. A., and D. D. Pollard (1995), Distinct element modeling of deformation bands in sandstone, *J. Struct. Geol.*, *17*, 1165–1182.
- Antonellini, M. A., A. Aydin, and D. D. Pollard (1994), Microstructure of deformation bands in porous sandstones at Arches National Park, Grand County, Utah, *J. Struct. Geol.*, *16*, 941–959.
- Armstrong, R. L. (1968), Sevier orogenic belt in Nevada and Utah, *Geol. Soc. Am. Bull.*, *79*, 429–458.
- Aydin, A. (1978), Small faults formed as deformation bands in sandstone, *Pure Appl. Geophys.*, *116*, 913–930.
- Aydin, A., and A. M. Johnson (1978), Development of faults as zones of deformation bands and as slip surfaces in sandstone, *Pure Appl. Geophys.*, *116*, 931–942.
- Baud, P., W. Zhu, and T.-f. Wong (2000), Failure mode and weakening effect of water on sandstone, *J. Geophys. Res.*, *105*, 16,371–16,390.
- Baud, P., E. Klein, and T.-f. Wong (2004), Compaction localization in porous sandstones: Spatial evolution of damage and acoustic emission activity, *J. Struct. Geol.*, *26*, 603–624.
- Bieniawski, Z. T. (1984), *Rock Mechanics Design in Mining and Tunneling*, 272 pp., A. A. Balkema, Brookfield, Vt.
- Blakey, R. C. (1989), Triassic and Jurassic geology of the southern Colorado Plateau, in *Geologic Evolution of Arizona*, edited by J. P. Jenny and S. J. Reynolds, *Ariz. Geol. Soc. Dig.*, *17*, 369–396.
- Bohannon, R. G. (1983), Mesozoic and Cenozoic tectonic development of the Muddy, North Muddy, and northern Black Mountains, Clark County, Nevada, *Mem. Geol. Soc. Am.*, *157*, 125–148.
- Brock, W. G., and T. Engleder (1979), Deformation associated with the movement of the Muddy Mountain overthrust in the Buffington window, southeastern Nevada, *Geol. Soc. Am. Bull.*, *88*, 1667–1677.
- Carpenter, J. A., and D. G. Carpenter (1994), Fold-thrust structure, synorogenic rocks, and structural analysis of the North Muddy and Muddy Mountains, Clark County, Nevada, in *Structural and Stratigraphic Investigations and Petroleum Potential of Nevada, With Special Emphasis South of the Railroad Valley Producing Trend*, edited by S. W. Dobbs and W. J. Taylor, pp. 65–94, Nev. Pet. Soc., Reno.
- Chester, J. S., S. C. Lenz, F. M. Chester, and R. A. Lang (2004), Mechanisms of compaction of quartz sand at diagenetic conditions, *Earth Planet. Sci. Lett.*, *220*(3-4), 435–451.
- Cocco, M., and J. R. Rice (2002), Pore pressure and poroelasticity effects in Coulomb stress analysis of earthquake interactions, *J. Geophys. Res.*, *107*(B2), 2030, doi:10.1029/2000JB000138.
- Crouch, S. L. (1976), Solution of plane elasticity problems by the displacement discontinuity method, *Int. J. Numer. Methods Eng.*, *10*, 301–343.
- Crouch, S. L., and A. M. Starfield (1983), *Boundary Element Methods in Solid Mechanics: With Applications in Rock Mechanics and Geological Engineering*, 322 pp., Allen and Unwin, London.
- Du Bernard, X., P. Eichhubl, and A. Aydin (2002), Dilation bands: A new form of localized failure in granular media, *Geophys. Res. Lett.*, *29*(24), 2176, doi:10.1029/2002GL015966.
- Eichhubl, P., W. L. Taylor, D. D. Pollard, and A. Aydin (2004), Paleo-fluid flow and deformation in the Aztec Sandstone at the Valley Of Fire Nevada—Evidence for the coupling of hydrogeological, diagenetic, and tectonic processes, *Geol. Soc. Am. Bull.*, *116*, 1120–1136.
- Eshelby, J. D. (1957), The determination of the elastic field of an ellipsoidal inclusion and related problems, *Proc. R. Soc. London, Ser. A*, *241*, 376–396.
- Eshelby, J. D. (1959), The elastic field outside an ellipsoidal inclusion, *Proc. R. Soc. London, Ser. A*, *252*, 561–569.
- Fletcher, R. C., and D. D. Pollard (1981), Anticrack model for pressure solution surfaces, *Geology*, *9*, 419–424.
- Flodin, E. A., and A. Aydin (2004a), Evolution of a strike-slip fault network, Valley of Fire, southern Nevada, *Geol. Soc. Am. Bull.*, *116*, 42–59.
- Flodin, E. A., and A. Aydin (2004b), Faults with asymmetric damage zones in sandstone, Valley of Fire State Park, southern Nevada, *J. Struct. Geol.*, *26*, 983–988.
- Flodin, E. A., M. Gerdes, A. Aydin, and W. D. Wiggins (2005), Petrophysical properties and sealing capacity of fault rock from sheared-joint based faults, Aztec Sandstone, Nevada, in *Fault Seals and Petroleum Traps*, edited by Y. Tsuji and R. Sorkhabi, *AAPG Mem.*, *85*, 197–217.
- Haimson, B. C. (2003), Borehole breakouts in Berea sandstone reveal a new fracture mechanism, *Pure Appl. Geophys.*, *160*, 813–831.

- Haimson, B. C., and H. Lee (2004), Borehole breakouts and compaction bands in two high-porosity sandstones, *Int. J. Rock Mech. Min. Sci.*, *41*, 287–301.
- Hill, R. E. (1989), Analysis of deformation bands in the Aztec Sandstone, Valley of Fire State Park, Nevada, Master's thesis, Univ. of Nev., Las Vegas.
- Hoagland, R. G., G. T. Hahn, and A. R. Rosenfield (1973), Influence of microstructure on fracture propagation in rock, *Rock Mech.*, *5*, 77–106.
- Issen, K. A., and J. W. Rudnicki (2000), Conditions for compaction bands in porous rock, *J. Geophys. Res.*, *105*, 21,529–21,536.
- Issen, K. A., and J. W. Rudnicki (2001), Theory of compaction bands in porous rock, *Phys. Chem. Earth*, *26*(1-2), 95–100.
- Karner, S. L., F. M. Chester, A. K. Kronenberg, and J. S. Chester (2003), Subcritical compaction and yielding of granular quartz sand, *Tectonophysics*, *377*, 357–381.
- Lawn, B. R. (1993), *Fracture of Brittle Solids*, 378 pp., Cambridge Univ. Press, New York.
- Longwell, C. R. (1949), Structure of the northern Muddy Mountain area, Nevada, *Geol. Soc. Am. Bull.*, *60*, 923–967.
- Marzolf, J. E. (1983), Changing wind and hydrologic regimes during deposition of the Navajo and Aztec sandstones, southwestern United States, in *Eolian Sediments and Processes*, *Dev. Sediment.*, vol. 38, edited by M. E. Brookfield and T. S. Ahlbrandt, pp. 635–660, Elsevier, New York.
- Mollema, P. N., and M. A. Antonellini (1996), Compaction bands; a structural analog for anti-mode I cracks in aeolian sandstone, *Tectonophysics*, *267*, 209–228.
- Morgan, J. K. (1999), Numerical simulations of granular shear zones using the distinct element method: 2. Effect of particle size distribution and interparticle friction on mechanical behavior, *J. Geophys. Res.*, *104*, 2721–2732.
- Morgan, J. K., and M. S. Boettcher (1999), Numerical simulations of granular shear zones using the distinct element method: I. Shear zone kinematics and micromechanics of localization, *J. Geophys. Res.*, *104*, 2703–2719.
- Mura, T. (1987), *Micromechanics of Defects in Solids*, Martinus Nijhoff, Hague, Netherlands.
- Myers, R., and A. Aydin (2004), The evolution of faults formed by shearing across joint zones in sandstone, *J. Struct. Geol.*, *26*, 947–966.
- Olsson, W. A. (1999), Theoretical and experimental investigation of compaction bands in porous rock, *J. Geophys. Res.*, *104*, 7219–7228.
- Olsson, W. A., and D. J. Holcomb (2000), Compaction localization in porous rock, *Geophys. Res. Lett.*, *27*, 3537–3540.
- Peck, L., C. C. Barton, and R. B. Gordon (1985), Microstructure and the resistance of rock to tensile fracture, *J. Geophys. Res.*, *90*, 11,533–11,546.
- Rudnicki, J. W. (1999), Alteration of regional stress by reservoirs and other inhomogeneities: Stabilizing or destabilizing?, in *Proceedings of the Ninth International Congress on Rock Mechanics*, edited by G. Vouille and P. Berest, pp. 1629–1637, Int. Soc. of Rock Mech., Paris.
- Sternlof, K., and D. Pollard (2001), Deformation bands as linear elastic fractures: Progress in theory and observation, *Eos Trans. AGU*, *82*(47), Fall Meet. Suppl., Abstract T42E-04.
- Sternlof, K., and D. Pollard (2002), Numerical modeling of compactive deformation bands as granular “anti-cracks”, *Eos Trans. AGU*, *83*(47), Fall Meet. Suppl., Abstract T11F-10.
- Sternlof, K., D. Pollard, and G. Chopra (2003), Compaction bands as anti-cracks in sandstone: Taming complexity through integrated observation, experimentation and process-based simulation, *Geol. Soc. Am. Abstr. Programs*, *35*(6), 40.
- Sternlof, K., J. Chapin, D. D. Pollard, and L. J. Durlafsky (2004), Effective permeability in sandstone containing deformation band arrays, *AAPG Bull.*, *88*, 1315–1329.
- Taylor, W. L., and D. D. Pollard (2000), Estimation of in-situ permeability of deformation bands in porous sandstone, Valley of Fire, Nevada, *Water Resour. Res.*, *36*, 2595–2606.
- Taylor, W. L., D. D. Pollard, and A. Aydin (1999), Fluid flow in discrete joint sets-field observations and numerical simulations, *J. Geophys. Res.*, *104*, 28,983–29,006.
- Tembe, S., V. Vajdova, T.-f. Wong, and W. Zhu (2005), Initiation and propagation of strain localization in circumferentially notched samples of two porous sandstone, *J. Geophys. Res.*, doi:10.1029/2005JB003611, in press.
- Townend, J., and M. D. Zoback (2000), How faulting keeps the crust strong, *Geology*, *28*, 399–402.
- Vajdova, V., and T.-f. Wong (2003), Incremental propagation of discrete compaction bands: Acoustic emission and microstructural observations on circumferentially notched samples of Bentheim sandstone, *Geophys. Res. Lett.*, *30*(14), 1775, doi:10.1029/2003GL017750.
- Weertman, J., and J. R. Weertman (1964), *Elementary Dislocation Theory*, 213 pp., Macmillan, New York.
- Wong, T., P. Baud, and E. Klein (2001), Localized failure modes in compactant porous rock, *Geophys. Res. Lett.*, *28*, 2521–2524.
- Zoback, M. D., and J. H. Healy (1984), Friction, faulting and “in situ” stress, *Ann. Geophys.*, *2*(6), 689–698.

D. D. Pollard and K. R. Sternlof, Department of Geological and Environmental Sciences, Stanford University, 450 Serra Mall, Bldg. 320, Stanford, CA 94305, USA. (kurtster@pangea.stanford.edu)

J. W. Rudnicki, Department of Civil and Environmental Engineering, Northwestern University, Evanston, IL 60208, USA.